Supplementary Information:

An ‘Atom-to-Circuit’ modeling approach to all-2D Metal-Insulator-Semiconductor Field-Effect Transistor

Biswapriyo Das and Santanu Mahapatra

A. Additional information on atomistic modeling

After optimizing the geometries of the unit cells of individual constituent materials, we obtain the in-plane lattice constants of graphene as $a = b \approx 2.472\ \text{Å}$, of hBN as $a = b \approx 2.525\ \text{Å}$ and $a = b \approx 3.192\ \text{Å}$ for MoS_2 (see Fig. S-1). Moreover, the bond lengths of those fully relaxed hexagonal unit cells were calculated considering all the X, Y and Z coordinates as $1.43\ \text{Å}$ (C–C) for graphene, $1.46\ \text{Å}$ (B–N) for hBN, and $2.44\ \text{Å}$ (Mo–S) and $3.19\ \text{Å}$ (S–S) for MoS_2 (see Fig. S-1). The direct bandgap of hBN is found to be 4.62 eV.

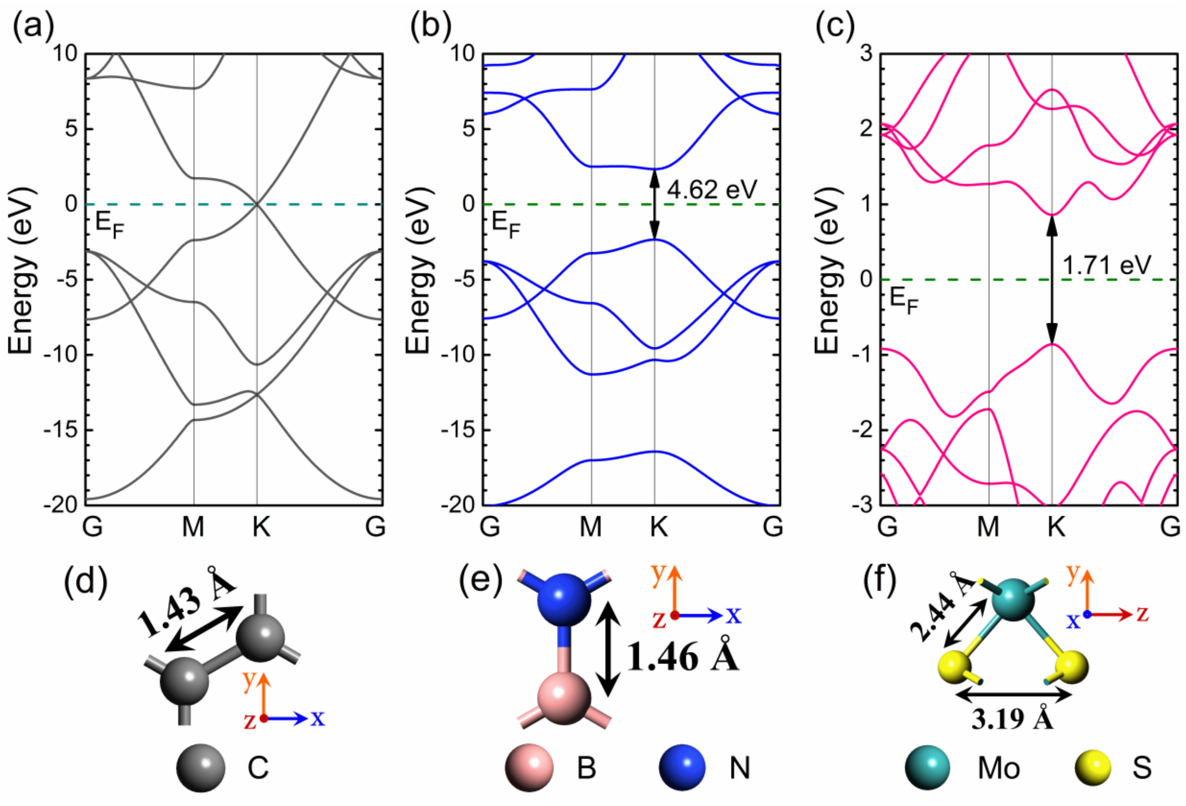

Fig. S-1: Band structure of unit cell of (a) graphene, (b) hBN, (c) MoS_2 with their quasiparticle bandgaps shown in corresponding figure. (d), (e) and (f) respectively depict the unit cell of graphene, hBN and MoS_2 along with their atomic bond lengths.

Among the several hetero-interfaces comprising of MoS_2 and hBN, it was observed that the structure with one N atom of hBN coinciding with one S atom of MoS_2, forming NS (N on top of S) configuration (see Fig. S-2), has the lowest binding energy (BE) of $-2.103\ \mathrm{eV}$; thereby making itself most stable configuration despite minute deviation of BEs for other configurations. Similarly for graphene-hBN interface, the Bernal-stacked structure with C atoms of one graphene sublattice residing right above B atoms of hBN while those of the other sublattice being at the center of hollow sites of BN hexagons (CB configuration) (see Fig. S-2), was found to be the ground state (with BE of $-2.77\ \mathrm{eV}$) as reported previously. This is due to the π-electron attractive interaction of the cation and repulsive interaction of the anion prevailing between graphene and hBN sheets. The N anions of hBN prefer to be located right below the hexagon-center of graphene, where there is negligible π-electron cloud, whereas the B cations locate themselves right below the C atoms to enhance the attractive interaction.

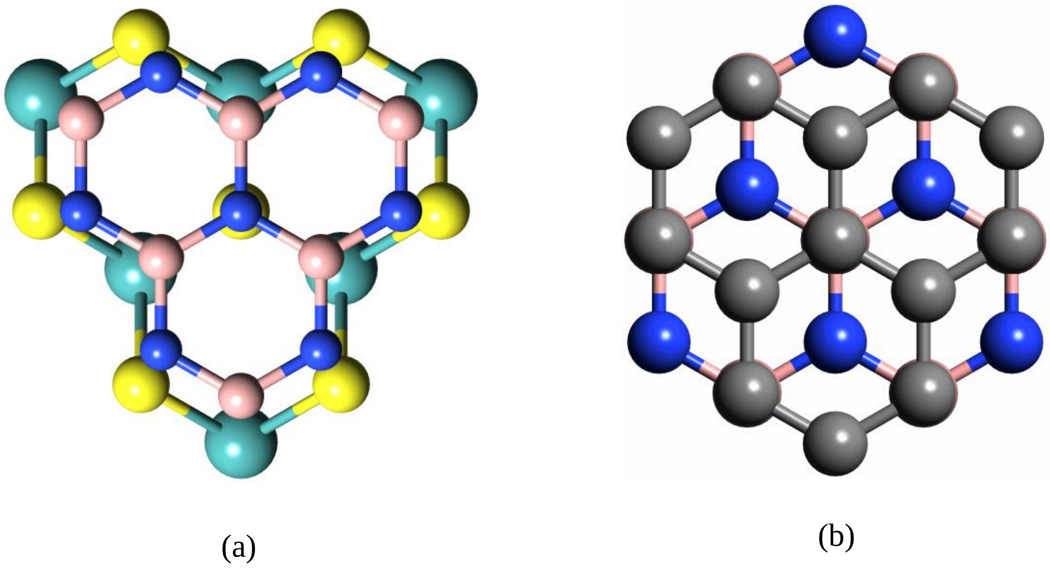

Fig. S-2: (a) NS stacking pattern of hBN on top of MoS2. (b) CB configuration of graphene over hBN. Color codes of the atoms are as follows: yellow: Sulphur, green: Molybdenum, blue: Nitrogen, pink: Boron, grey: Carbon.

B. Band structures of graphene-hBN and MoS2-hBN vdWHs

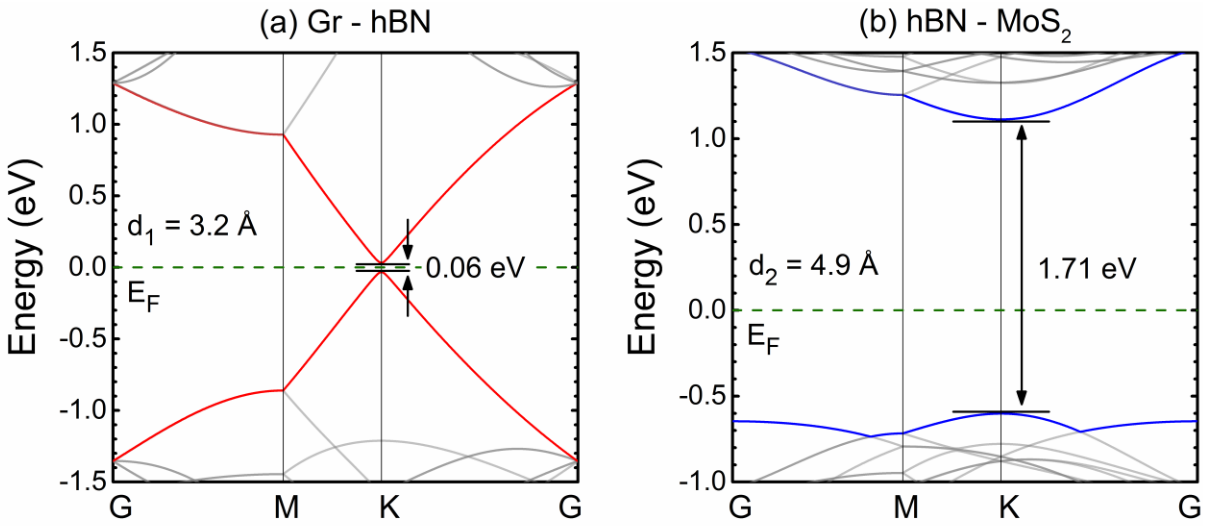

Fig. S-3: Electronic band structure of (a) graphene-hBN, (b) hBN-MoS2 vdW Heterostructures at their equilibrium interlayer spacings. In (a), red bands are contributed by graphene and in (b), blue bands are contributed by MoS$_2$.

C. Fat-Band structure of graphene-hBN-MoS2 vdWH

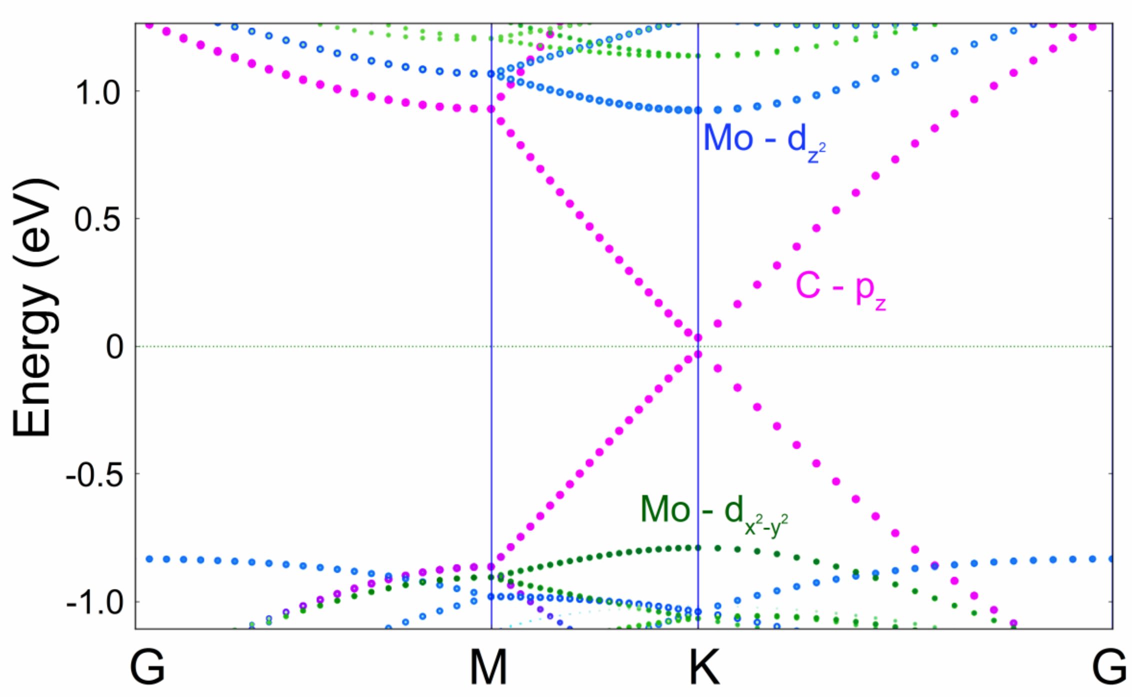

Fig. S-4: The Fat band structure of graphene-hBN-MoS$_2$ vdWH. It reveals that the CBM and VBM of graphene are mostly contributed by Carbon p_z orbitals, and for MoS$_2$, CBM is mostly composed of Mo d_{z^2} orbital, whereas VBM is mainly made of Mo $d_{x^2-y^2}$ orbital.

D. Details of piecewise charge linearization (PWCL) technique

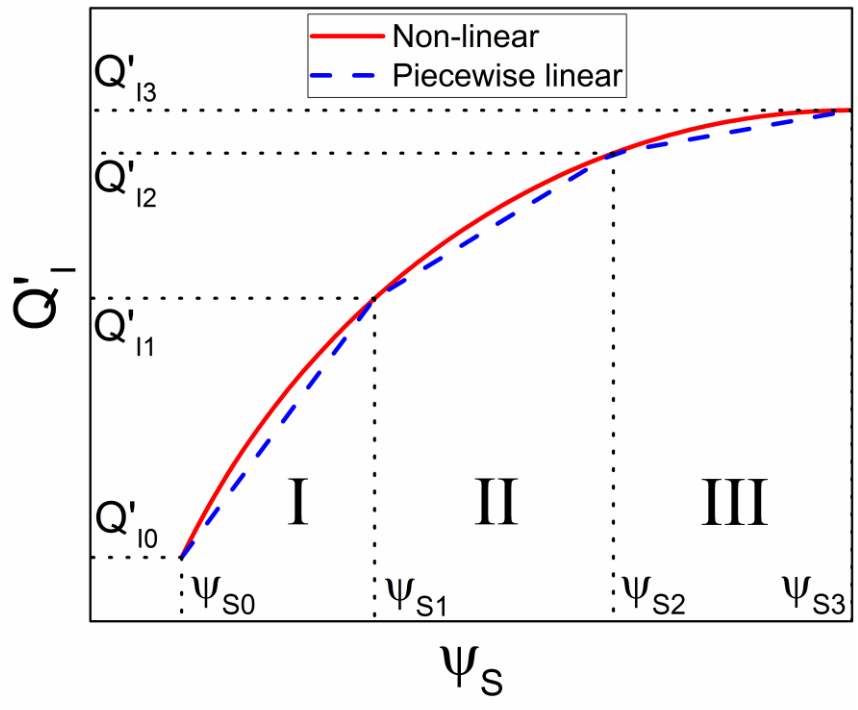

Fig. S-5: Demonstration of piecewise charge linearization technique by selecting two break points in the channel. The red curve is the actual non-linear relationship between Q_I' and ψ_S, whereas the blue dashed line is its piecewise linear approximation.

The piecewise charge linearization scheme is depicted in Fig. S-5 (not to scale; only for demonstration purpose). In DD formalism, the dc drain current equation can be written as:

$$I_{DC} = \frac{W}{L}\left[\mu\int_{\psi_{S0}}^{\psi_{SL}}\left(-Q_I'\right)d\psi_S + D\int_{Q_{I0}'}^{Q_{IL}'} dQ_I'\right] \tag{S1}$$

The bias dependent diffusivity D, calculated as $D = \mu Q_I'\left(d\psi_S \big/ dQ_I'\right)\Big|_{V_{DS}=0}$ has the following form:

$$D = \mu\frac{KT}{q}\times\frac{\left[g_{Mn}\ln\left\{1+\exp\left(-\frac{\Delta_{MC}}{KT}+\frac{q\psi_S}{KT}-\frac{qV_{CB}}{KT}\right)\right\}-g_{Mp}\ln\left\{1+\exp\left(-\frac{\Delta_{MV}}{KT}-\frac{q\psi_S}{KT}\right)\right\}\right]}{\left[g_{Mn}\left\{1+\exp\left(\frac{\Delta_{MC}}{KT}-\frac{q\psi_S}{KT}+\frac{qV_{CB}}{KT}\right)\right\}^{-1}+g_{Mp}\left\{1+\exp\left(\frac{\Delta_{MV}}{KT}+\frac{q\psi_S}{KT}\right)\right\}^{-1}\right]} \tag{S2}$$

In order to obtain a closed form expression of I_{DC}, Q_I' as a function of ψ_S should be integrable analytically. But in this case, the non-linear transcendental relation between Q_I' and ψ_S (as cartooned in Fig. S-5) necessitates a charge linearization scheme, whereby we approximate Q_I' as a piecewise linear function of ψ_S facilitating closed form expression of I_{DC}. To tackle significant nonlinearity (originated from the band gap opening in graphene) of the relation, we divide the whole MISFET channel into three segments by carefully selecting two break points between ψ_{S0} and ψ_{SL} ($\equiv \psi_{S3}$) as shown in Fig. S-5. Incorporation of more number of break points increases the accuracy of the approximation at the cost of computational budget (as we have to solve the surface potential equation (F1) at each break point). We found that selecting only two break points (one at $3\left(\psi_{S0}+\psi_{S3}\right)/4 \equiv \psi_{S1}$ and another at $\left(\psi_{S1}+\psi_{S3}\right)/2 \equiv \psi_{S2}$) makes a good balance between the accuracy and the computational cost as shown in Fig. S-6. In Fig. S-7, we show that proposed model without any break points fits well with the exact drain current value for $d_1 = 3.4$ Å (i.e., when bandgap opening in graphene is negligible). This is equivalent to industry standard models (e.g. PSP, EKV) for Si-MOSFET with conventional gate stack, where no breakpoint is used. It is worth noting that these selected break points are independent of device parameters and external biases. The steps for computation of drain current and terminal charges are described as follows:

I. For a given bias condition (i.e. V_{GS} and V_{DS}), we numerically solve Eqn. (F1) of Fig. 5, i.e.

$$\zeta\left(V_{GS}, V_{CB}, \Delta_{GC}, \Delta_{GV}, \Delta_{MC}, \Delta_{MV}, m_{eG}^*, m_{hG}^*, m_{eM}^*, m_{hM}^*, \psi_S\right) = 0 \qquad \text{(S3)}$$

for ψ_S to obtain the values of $\psi_{S0}\left(\psi_S\big|_{V_{CB}=0}\right)$ and $\psi_{S3}\left(\psi_S\big|_{V_{CB}=V_{DS}}\right)$.

II. Then we calculate the values of $Q_{I0}{}'$ and $Q_{I3}{}'$ for those bias conditions using the relation: $Q_I{}' = q\left(p_{netM} - n_{netM}\right)$, where

$$n_{netM} = g_{Mn} KT \ln\left[1 + \exp\left(-\frac{\Delta_{MC}}{KT} + \frac{q\left(\psi_S - V_{CB}\right)}{KT}\right)\right] \tag{S4}$$

$$p_{netM} = g_{Mp} KT \ln\left[1 + \exp\left(-\frac{\Delta_{MV}}{KT} - \frac{q\psi_S}{KT}\right)\right] \tag{S5}$$

III. Then we select first break point ψ_{S1} at $\psi_S = \left(\psi_{S0} + \psi_{S3}\right)/2$ and second break point ψ_{S2} at $\psi_S = \left(\psi_{S1} + \psi_{S3}\right)/2$ (see Fig. S-5).

IV. In order to compute I_{DC} and terminal charges, this linearization scheme requires the values of $Q_I{}'$ at those break points, which is achieved through solving Eqn. (S3) for V_{CB} (ψ_S is known here) and thereby calculating $Q_{I1}{}'$ and $Q_{I2}{}'$ as deduced in step II.

V. Now that we have the values of $Q_{I_n}{}'$ and $\psi_{S_n}{}'$ ($n = 0,\ 1,\ 2,\ 3$) at the break points, we can join those points to get the piecewise linearized graph and hence, the expression for I_{DC} can be rewritten as:

$$I_{DC} = \frac{W}{L}\mu\left\{\int_{\psi_{S0}}^{\psi_{S1}}\left(-Q_I{}'\right)d\psi_S + \int_{\psi_{S1}}^{\psi_{S2}}\left(-Q_I{}'\right)d\psi_S + \int_{\psi_{S2}}^{\psi_{S3}}\left(-Q_I{}'\right)d\psi_S\right\} + \frac{W}{L}D\left(Q_{I3} - Q_{I0}\right) \tag{S6}$$

The integrals in Eqn. (S6) can be analytically computed using the linear relations:

$$Q_I{}' = \left(Q_{I_n}{}' - \frac{Q_{I_n}{}' - Q_{I_{n-1}}{}'}{\psi_{S_n} - \psi_{S_{n-1}}}\psi_{S_n}\right) + \frac{Q_{I_n}{}' - Q_{I_{n-1}}{}'}{\psi_{S_n} - \psi_{S_{n-1}}}\psi_S \tag{S7}$$

where $n = 1, 2, 3$ and the value of n indicates that n^{th} expression of Q_I' needs to be put in n^{th} integral of Eqn. (S6). After few algebraic calculations, we get the final closed form I_{DC} as shown in Eqn. (F2) of Fig. 5.

VI. Thereafter in order to obtain the closed form expressions of terminal charges, we first define

$$f_{\psi_{SL}} = \left[\int_{\psi_{S0}}^{\psi_{SL}} \mu \left(-Q_I' \right) d\psi_S + \int_{Q_{I0}'}^{Q_{IL}'} D dQ_I' \right] \tag{S8}$$

which can be rewritten in compact form as:

$$f_{\psi_{SL}} = \sum_{n=1}^{3} \left\{ -\frac{\mu}{2} \left(\psi_{S_n} - \psi_{S_{n-1}} \right) \left(Q'_{I_n} + Q'_{I_{n-1}} \right) + D \left(Q'_{I_n} - Q'_{I_{n-1}} \right) \right\} \tag{S9}$$

Thus $I_{DC} = \left(W/L \right) f_{\psi_{SL}}$. This function $f_{\psi_{SL}}$ is defined at $x = L$, i.e. at drain terminal. Similarly, we can define a function $f_{\psi_{Sx}}$ for any point x in the channel lying in any of the three segments separated by the break points. After some algebra, we get three expressions for $f_{\psi_{Sx}}$, defined in segment I, II and III respectively as:

$$f_{\psi_{Sx}} \Big|_{[\mathrm{I}]} = -\mu \left\{ c_1 \left(\psi_{Sx} - \psi_{S0} \right) + \frac{1}{2} m_1 \left(\psi_{Sx}^{\ 2} - \psi_{S0}^{\ 2} \right) \right\} + D \left(Q_{Ix}' - Q_{I0}' \right) \tag{S10}$$

$$\begin{aligned} f_{\psi_{Sx}} \Big|_{[\mathrm{II}]} = & -\mu \left\{ c_1 \left(\psi_{S1} - \psi_{S0} \right) + \frac{1}{2} m_1 \left(\psi_{S1}^{\ 2} - \psi_{S0}^{\ 2} \right) + c_2 \left(\psi_{Sx} - \psi_{S1} \right) + \frac{1}{2} m_2 \left(\psi_{Sx}^{\ 2} - \psi_{S1}^{\ 2} \right) \right\} \\ & + D \left(Q_{Ix}' - Q_{I0}' \right) \end{aligned} \tag{S11}$$

$$\begin{aligned} f_{\psi_{Sx}} \Big|_{[\mathrm{III}]} = & -\mu \left\{ \begin{aligned} & c_1 \left(\psi_{S1} - \psi_{S0} \right) + \frac{1}{2} m_1 \left(\psi_{S1}^{\ 2} - \psi_{S0}^{\ 2} \right) + c_2 \left(\psi_{S2} - \psi_{S1} \right) + \frac{1}{2} m_2 \left(\psi_{S2}^{\ 2} - \psi_{S1}^{\ 2} \right) \\ & + c_3 \left(\psi_{Sx} - \psi_{S2} \right) + \frac{1}{2} m_3 \left(\psi_{Sx}^{\ 2} - \psi_{S2}^{\ 2} \right) \end{aligned} \right\} \\ & + D \left(Q_{Ix}' - Q_{I0}' \right) \end{aligned} \tag{S12}$$

where, ψ_{Sx} and $Q_{Ix}{}'$ are the values of ψ_S and $Q_I{}'$ at position x respectively, and

$$c_n = Q_{I_n}{}' - \frac{Q_{I_n}{}' - Q_{I_{n-1}}{}'}{\psi_{S_n} - \psi_{S_{n-1}}}\psi_{S_n} \quad ; \quad m_n = \frac{Q_{I_n}{}' - Q_{I_{n-1}}{}'}{\psi_{S_n} - \psi_{S_{n-1}}} \quad (n = 1, 2, 3) \tag{S13}$$

VII. Due to continuity of current in the channel, $I_{DC} = (W/x)\, f_{\psi_{Sx}}$ and thus,

$$x = L\frac{f_{\psi_{Sx}}}{f_{\psi_{SL}}} \tag{S14}$$

VIII. Now we calculate the terminal charge Q_G as:

$$Q_G = -W\int_0^L Q_{Ix}{}'(x)\,dx \tag{S15}$$

To evaluate this integral in Eqn. (S15), we rewrite it as:

$$Q_G = -W\sum_{n=1}^{3}\left\{\int_{\psi_{S_{n-1}}}^{\psi_{S_n}} Q_{Ix}{}'(x)\frac{dx}{d\psi_{Sx}}\,d\psi_{Sx}\right\} \tag{S16}$$

where, $Q_{Ix}{}'(x)$ in n^{th} segment is given as $Q_{Ix}{}'(x) = c_n + m_n\psi_{Sx}$ and the expression for $\frac{dx}{d\psi_{Sx}}$ in n^{th} segment is obtained as: $\frac{dx}{d\psi_{Sx}} = \frac{L}{f_{\psi_{SL}}}\left(-\mu c_n + Dm_n - \mu m_n\psi_{Sx}\right)$. The final form of Q_G is shaped in Eqn. (F3) of Fig. 5.

IX. To calculate the terminal charge Q_D, we rewrite the equation $Q_D = W\int_0^L \frac{x}{L} Q_{Ix}{}'(x)\,dx$ as

$$Q_D = W\sum_{n=1}^{3}\left\{\int_{\psi_{S_{n-1}}}^{\psi_{S_n}} \left(\frac{x}{L}\right) Q_{Ix}{}'(x)\frac{dx}{d\psi_{Sx}}\,d\psi_{Sx}\right\} \tag{S17}$$

and the integrations are carried out replacing $\frac{x}{L}$ from Eqn. (S14). After rigorous algebraic manipulation, the final form of Q_D is obtained as what is shaped in Eqn. (F4) of Fig. 5.

X. Finally, terminal charge Q_S is calculated as $Q_S = -\left(Q_G + Q_D\right)$.

E. Comparison between numerical and analytical models

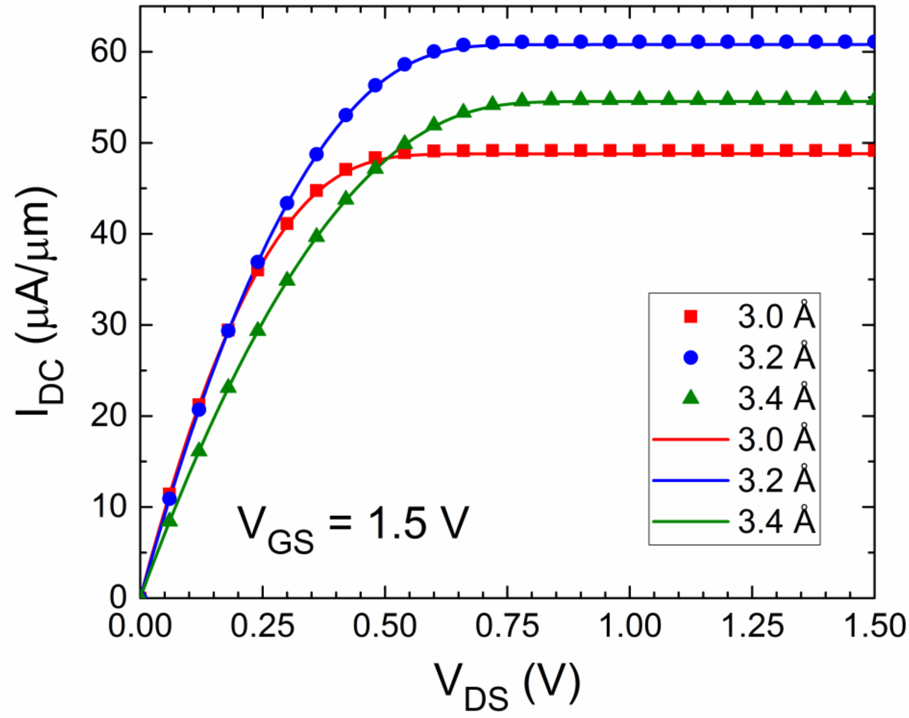

Fig. S-6: Comparison between exact numerical values of Eqn. (S1) as represented by symbols and the values obtained from analytical solution (Eqn. (F2) of Fig. 5) as denoted by lines.

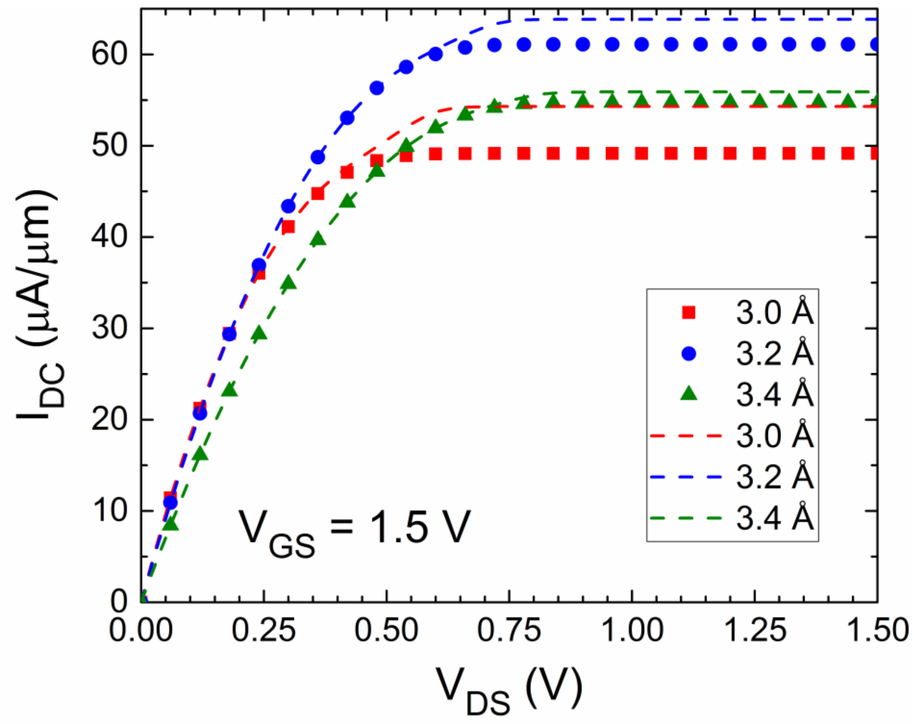

Fig. S-7: Comparison between exact numerical values of Eqn. (S1) as represented by symbols and the values obtained from analytical solution (Eqn. (F2) of Fig. 5) with no intermediate break point as denoted by lines. It shows that piecewise linear approximation improves with incorporation of break points as compared with the results in figure S-6.

F. Current-voltage characteristics of the vdWH-based MISFET with doped MoS_2 layer

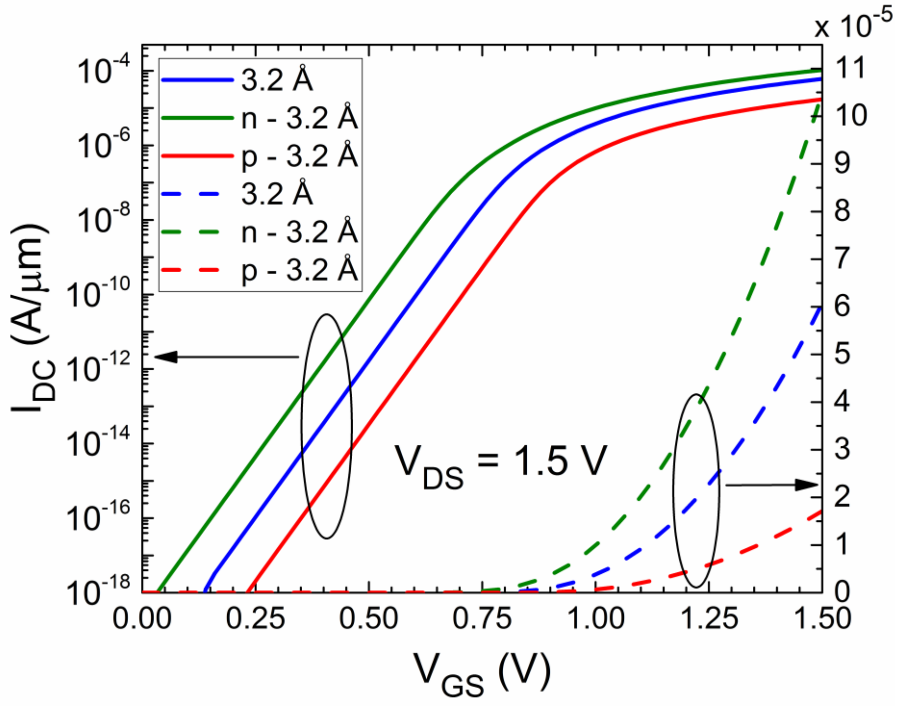

Fig. S-8: Comparison between drain current vs. gate voltage plots of the vdWH-based MISFETs with undoped MoS_2 layer and n-type and p-type doped MoS_2 layers. It shows that the subthreshold slope of the device remains unaltered with respect to doping, although the drain current increases significantly for n-type doped MoS_2 and conversely reduces with p-type doping. Also it is observed that the threshold voltage of the device reduces for n-type doping and it increases for p-type doping. For all three cases, graphene and hBN layers were separated at the equilibrium interlayer distance of 3.2 Å.

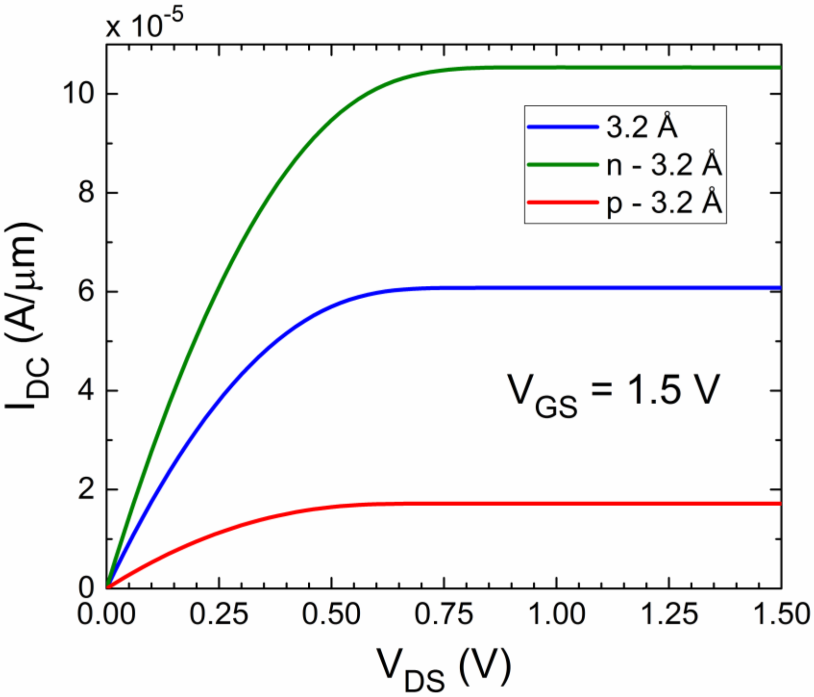

Fig. S-9: Comparison between drain current vs. drain voltage plots of the vdWH-based MISFETs with undoped MoS_2 layer and n-type and p-type doped MoS_2 layers. Clearly observed is the increment of drain current with n-type doping and conversely its reduction with p-type doping in MoS_2. For all three cases, graphene and hBN layers were separated at the equilibrium interlayer distance of 3.2 Å.